Chemical Science

ROYAL SOCIETY OF CHEMISTRY

EDGE ARTICLE

View Article Online
View Journal

Cite this: DOI: 10.1039/d5sc09242f

All publication charges for this article have been paid for by the Royal Society of Chemistry

Tailoring terminal groups in sulfonyl solvents to boost compatibility with lithium metal anodes

Jinmin Wang, †[a] Shuang Wei,†[bc] Mingming Fang,*[b] Angye Li,[d] Qian Zheng,[a] Xubing Dong,[b] Yuanmao Chen,[b] Kang Yuan,[b] Xinyang Yue*[b] and Zheng Liang *[b]

Sulfonyl-based compounds are considered promising electrolyte solvents because of their high dielectric constant, excellent anodic stability, and non-flammability. However, their use in Li metal batteries (LMBs) is limited by their incompatibility with Li, causing unstable interfacial chemistry and dendrite growth. Herein, we designed an *N*,*N*-dimethylsulfamoyl fluoride (DMSF) electrolyte by functionalizing a fluorosulfonyl (FSO_2^-) core with an *N*,*N*-dimethyl terminal group, enabling the LMB with enhanced cycling stability and energy density. The increased steric hindrance in DMSF with methylation weakens the interaction with Li ions, resulting in a structure that is weakly solvating and exhibits fast ion transport kinetics. Methylation also facilitates the decomposition of DMSF, leading to the formation of a rich LiF/Li_2S hybrid solid electrolyte interphase that suppresses interfacial side reactions. Consequently, the 4.5 V-charged 50 μm Li||$LiNi_{0.8}Co_{0.1}Mn_{0.1}O_2$ (4 mAh cm^{-2}) cells exhibit stable cycling (80% capacity retention for 850 cycles), 5C fast charging, and a wide operating temperature range (−50–60 °C). Moreover, a 5-Ah pouch cell employing DMSF delivers an energy density of 540 Wh kg^{-1} and exhibits high stability over 110 cycles. This study establishes terminal group modification as a crucial advance for developing compatible sulfonyl-based electrolytes in high-performance LMBs.

Received 26th November 2025
Accepted 3rd January 2026

DOI: 10.1039/d5sc09242f

rsc.li/chemical-science

1 Introduction

Lithium metal batteries (LMBs) are of considerable strategic importance for advancing high-energy-density energy storage systems. The core advantage lies in the Li metal anode, which boasts an extremely high theoretical specific capacity of 3860 mAh g^{-1} and the lowest electrochemical potential of −3.04 V *versus* the standard hydrogen electrode.[1–4] Nevertheless, the high reactivity between Li metal and organic electrolytes, particularly carbonate-based systems, leads to persistent irreversible side reactions during cycling, resulting in the formation of porous Li dendrites, the accumulation of dead Li, and the consumption of electrolytes, severely compromising the cycling life and safety of LMBs.[5–7] These issues are generally exacerbated when operating under extreme conditions such as high voltage, fast charging, and wide temperature ranges.[8–10] To address these challenges, the design of functional electrolytes has emerged as a promising strategy for modulating the Li-ion solvation structure and altering the composition of the solid-electrolyte interphase (SEI).[11–15] Representative approaches include using (localized) high-concentration electrolytes,[16–19] fluorinated electrolytes,[20–22] and high-entropy electrolytes,[23,24] which facilitate the formation of a uniform and thin SEI with anion-derived inorganic components.

Compared to the carbonyl group in carbonate solvents and the ether group in oligoethers, the strongly electron-withdrawing sulfonyl group significantly lowers the highest occupied molecular orbital (HOMO) energy level, thereby improving oxidation stability.[25–28] However, using sulfonyl-based solvents in LMBs is still problematic because they have poor wettability and high viscosity and struggle to form a stable SEI on Li anodes.[29–31] To enhance the compatibility, employing localized high-concentration electrolytes (LHCEs) or introducing functional groups into sulfonyl molecules has been demonstrated as an effective strategy with intriguing progress.[32,33] Incorporating an *N*,*N*-dimethyl group into trifluoromethyl-containing sulfonyls can yield an electrolyte exhibiting good compatibility with both Li metal (coulombic efficiency > 99%) and high-voltage cathodes (>4.7 V *vs.* Li/Li^+). Nevertheless, the combined steric hindrance from trifluoromethyl and *N*,*N*-dimethyl groups often reduces ionic conductivity at room temperature (1.5 mS cm^{-1}), limiting ion transport and rate performance.[34] Although Zhao and Kim *et al.* improved conductivity *via* mono-fluoro substitution, the electrochemical stability window was constrained to 4.3 V, which reduces the energy density of LMBs.[35,36] In essence, innovative sulfonyl-based electrolytes that simultaneously achieve high

[a]*School of Petrochemical Engineering, Changzhou University, Changzhou 213164, China*

[b]*Frontiers Science Center for Transformative Molecules, School of Chemistry and Chemical Engineering, Shanghai Jiao Tong University, Shanghai 200240, China. E-mail: 193679@sjtu.edu.cn; xinyangyue@sjtu.edu.cn; Liangzheng06@sjtu.edu.cn*

[c]*Shanghai TANSUO Testing and Inspection Company, Shanghai 200240, China*

[d]*Xi'an Jiaotong-Liverpool University, Suzhou 215000, China*

† These authors contributed equally to this work.

energy density, superior rate performance, and wide temperature tolerance remain scarce yet are critically demanded for long-cycling, high-energy-density LMBs.

In this work, *N*,*N*-dimethylsulfamoyl fluoride (DMSF) characterized by the introduction of an *N*,*N*-dimethyl terminal group onto a fluorosulfonyl (FSO_2^-) core was proposed to improve compatibility between sulfonyl solvents and Li metal. The DMSF electrolyte was formulated by combining lithium bis(fluorosulfonyl)imide (LiFSI) and lithium hexafluorophosphate ($LiPF_6$) at a molar ratio of LiFSI : $LiPF_6$: DMSF = 1 : 0.1 : 5 (1.6 mol L^{-1}). The synergistic integration of monofluoro and dimethyl functional groups imparts unique electronic and steric effects to the DMSF molecule. This configuration yields a weakly solvating structure that retains moderate oxidation stability while overcoming the high viscosity and poor wettability of conventional sulfonyl electrolytes. In addition, the investigation of the steric-hindrance-induced reductive decomposition of DMSF demonstrates that the electron-donating effect of the methyl groups delocalizes the electron density around the nitrogen atom, lowering the LUMO energy level of DMSF and promoting its preferential reduction to form a hybrid LiF/Li_2S-rich SEI. As a result, the improvement of the Li metal in terms of cycling is evident in the DMSF electrolyte, where the uniform Li^+ deposition significantly suppressed the dendrite growth. In the 50 μm Li‖$LiNi_{0.8}Co_{0.1}Mn_{0.1}O_2$ (NCM811) cell, stable cycling over 850 cycles (80% retention) at 4.5 V is achieved by using DMSF-electrolyte. This cell also delivers a specific capacity of 2.0 and 3.6 mAh at −50 and 60 °C (*vs.* 3.5 mAh at 25 °C), respectively, and could reversibly operate for 100 cycles. To validate the application of DMSF, a 5 Ah Li‖NCM811 pouch cell is assembled and showcases a competitive performance containing an energy density of 540 Wh kg^{-1} with 83.2% capacity retention after 110 cycles.

2 Introduction

2.1 Design of DMSF for LMB electrolyte

Replacing an alkyl group (R_1) with a trifluoromethyl group has been shown to yield fluorinated sulfonyl-based electrolytes with reduced viscosity.[34] However, the $-CF_3$ regulation to enhance stability toward Li metal is still insufficient for practical use under extreme conditions. Given the influence of solvent size and interaction on Li^+ transport in liquid electrolytes, a monofluoro substitution strategy instead of trifluoromethylation was involved in designing the electrolyte to provide a viable route toward electrolytes with good wettability and high ionic conductivity (Fig. 1, S1 and Table S1). On the other hand, introducing a tertiary amine group to form a sulfonamide structure can enhance compatibility with Li metal.[35] The two $-CH_3$ groups on the tertiary amine not only eliminate active hydrogen but also create a steric hindrance effect that delocalizes the electron density around the nitrogen atom, facilitating solvent decomposition under reductive conditions.

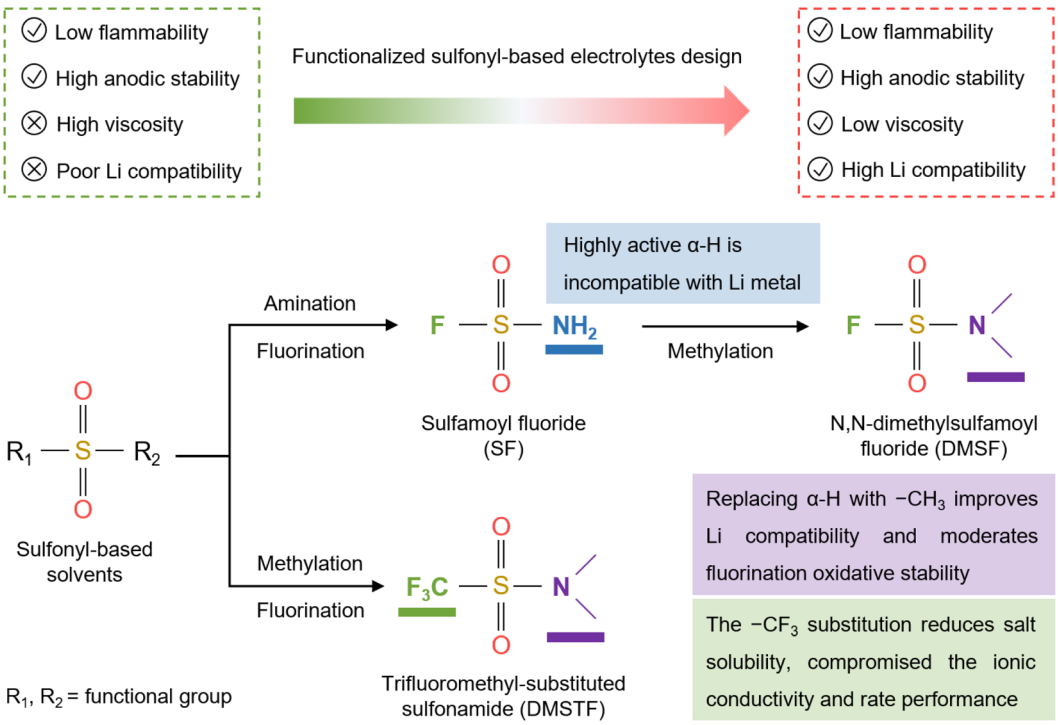

Fig. 1 Functionalization of sulfonyl-based molecules improves their compatibility with Li metal anodes. Trifluoromethyl modification reduces the viscosity and melting point of sulfonyls while boosting their oxidative stability. However, the strong electron-withdrawing nature of trifluoromethyl groups limits ionic conductivity and rate performance. To overcome this, monofluoro substitution is employed, reducing solvent molecular size and enabling the development of electrolytes with lower viscosity, higher ionic conductivity, and improved interfacial stability. Furthermore, the incorporation of a tertiary amine group to form a sulfonamide structure significantly enhances lithiophilicity. The two $-CH_3$ groups on the tertiary amine can eliminate active hydrogen and stabilize the Li metal anode.

To validate the above strategy, *N*,*N*-dimethylsulfamoyl fluoride (DMSF) was designed as a functional sulfonyl solvent for the LMB electrolyte. DMSF was synthesized *via* a nucleophilic substitution reaction, in which dimethylsulfamoyl chloride was reacted with antimony trifluoride at 60 °C for 24 h under stirring, followed by distillation and purification. As controls, sulfamoyl fluoride (SF) and trifluoromethyl-substituted sulfonamide (DMSTF) were prepared to investigate the effect of $-CH_3$ and $-CF_3$ groups on DMSF. (Fig. S2, detailed procedures are provided in the Experimental section). To balance ionic conductivity and cost, the electrolyte was formulated with LiFSI, $LiPF_6$, and DMSF at a molar ratio of 1 : 0.1 : 5 (1.6 mol L^{-1}). The $LiPF_6$ additive helps form a stable passivation film on the surface of aluminum foil, improving the stability of the cathode during cycling at a high charge cut-off voltage. The electrolytes based on DMSF, SF, and DMSTF are denoted as FSI/PF-DMSF, FSI/PF-SF, and FSI/PF-DMSTF, respectively.

2.2 Properties and the solvation structure of electrolytes

The electrochemical oxidation stability of electrolytes was evaluated in a Li||Al half-cell by linear sweep voltammetry (LSV) measurement. As shown in Fig. 2a, a significant oxidation current response (~4.3 V *vs.* Li/Li^+) suddenly appeared in the FSI-DMSF cell, indicating the Al corrosion by the FSI^- anion. With the $LiPF_6$ additive, both FSI/PF-DMSF and FSI/PF-SF show improved oxidation stability at ~5.5 V, demonstrating not only the passivation effect of PF_6^- but also the stable chemical structure of DMSF and SF. From the density functional theory (DFT) calculations (Fig. S3), the high antioxidant stability of the two solvents stems from the high band gap and low highest occupied molecular orbital (HOMO) energy level.

The reduction behavior of each electrolyte was studied in the Li||Cu half-cell by cyclic voltammetry (CV) measurement. The result reveals that the methylation of the α-H atom in DMSF significantly suppressed the reduction current (Fig. 2b). Previous research indicates that the α-H of electrolytes is one of the culprits of unstable LMB cycling. When Li metal comes into contact with FSI/PF-SF containing α-H, a violent reductive decomposition occurs, while the Li metal immersed in FSI/PF-DMSF was stable (Fig. S4). More importantly, compared to SF, the steric hindrance effect resulting from the dimethyl group facilitates the dispersion of electronic clouds on DMSF (2.43 V) by delocalizing the electron density around the nitrogen atom, leading to a higher reduction potential. The calculation of electrostatic distribution and the lowest unoccupied molecular orbital (LUMO) energy levels (Fig. S3 and S5) also confirms the above result. Therefore, it is inferred that a stable SEI can be quickly formed on the Li metal surface through the prior

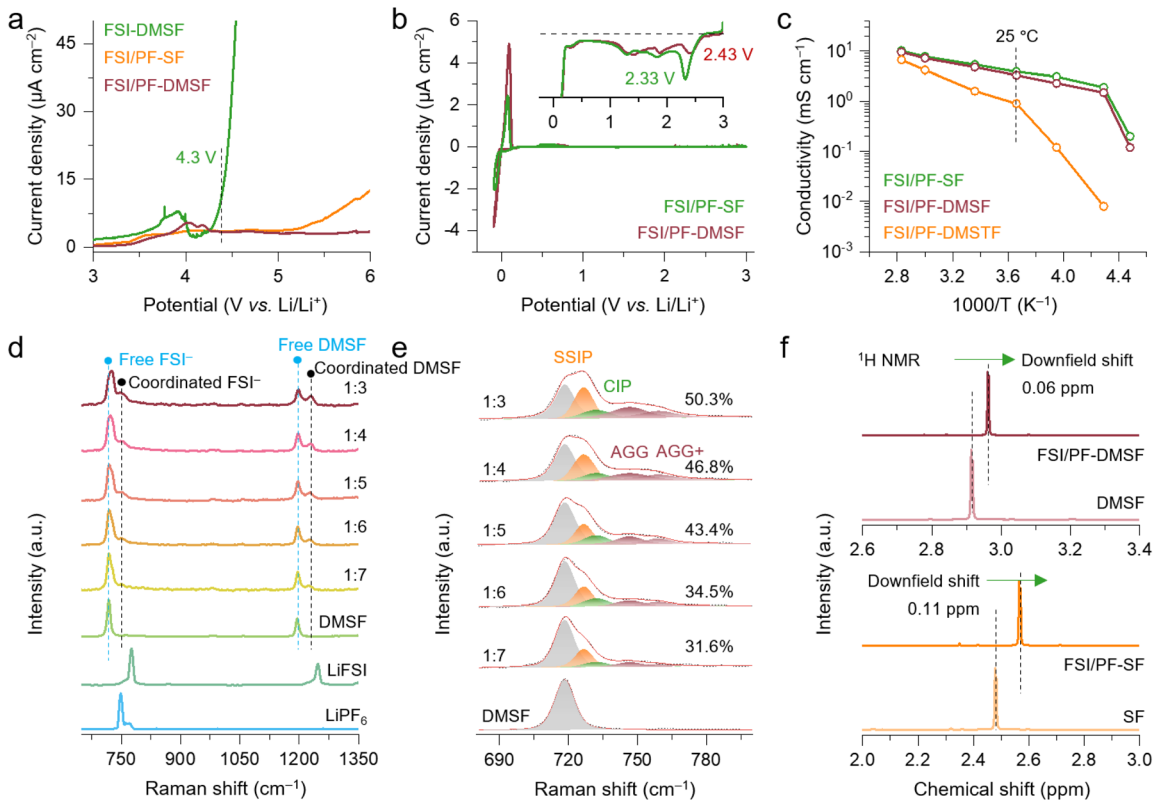

Fig. 2 Physicochemical properties and solvation structures of the fluorinated sulfonyl-based electrolytes. (a) LSV anodic scanning in Li||Al half cells at a scan rate of 0.2 mV s^{-1}. (b) CV cathodic scanning in the Li||Cu half cells at a scan rate of 0.1 mV s^{-1}. (c) Ionic conductivity measured at different temperatures. (d) Raman spectra of $LiPF_6$, LiFSI, DMSF, and FSI/PF-DMSF electrolytes with different molar ratios. (e) Fitted Raman spectra of FSI/PF-DMSF electrolytes with different molar ratios in the wavelength range from 680 to 800 cm^{-1}. It shows the ratio of the SSIP, CIP, and AGG in the solvation structure of FSI/PF-DMSF as a function of concentration. (f) ^1H NMR spectra of SF and DMSF solvents and FSI/PF-SF and FSI/PF-DMSF electrolytes.

reduction of DMSF, thereby restraining the severe reduction of electrolytes at low potential (high energy).

The ionic conductivity of the electrolyte was evaluated at different temperatures. Compared to FSI/PF-DMSTF, a higher ionic conductivity was achieved by FSI/PF-DMSF and FSI/PF-SF (Fig. 2c), which demonstrates that the large molecular size caused by methylation has a lower impact on ion transport of the electrolyte compared to $-CF_3$ substitution. In general, the hydrogen (H) bonding between SF is a key factor leading to a decrease in conductivity. For DMSF, despite the H-bonding effect being reduced, it has a larger molecular size than SF. Therefore, under the combined influence of these two factors, FSI/PF-DMSF and FSI/PF-SF exhibit similar ionic conductivity. However, the $-CF_3$ substitution further increases the solvent size of DMSTF, breaking the balance between molecular size and H-bonding effect in DMSF. Thus, FSI/PF-DMSTF shows the lowest ionic conductivity among the studied electrolytes. Besides, the ionic conductivity of FSI/PF-DMSF is 4.8, 3.3, 2.3, 1.5, and 0.12 mS cm^{-1} at 25, 0, −20, −40, and −50 °C, respectively. In view of the room-temperature ionic conductivity of the local high-concentration electrolyte (LHCE, Li salt concentration: 1–1.5 M), located at 1–2 mS cm^{-1}, FSI/PF-DMSF shows potential to enable the cell with stable operation across a wide temperature range. It should be mentioned that FSI/PF-DMSF retains the non-flammable properties of the sulfonyl-based electrolyte (Fig. S6).

The solvation structure of FSI/PF-DMSF was investigated using Raman and nuclear magnetic resonance (NMR) spectra. As shown in Fig. 2d, the S–N–S stretching vibration mode of the FSI^- anion is observed in the 680–800 cm^{-1} frequency range.[37,38] The spectra were deconvoluted to peaks centered at ~726, 732, 746, and 759 cm^{-1}, respectively, for assigning to the solvent-separated ion pair (SSIP), contact ion pair (CIP), and aggregate (AGG).[35] The fraction of the SSIP decreases from 49.8% (1 : 7) to 34.6% (1 : 3), whereas the fraction of the AGG increases from 31.6 (1 : 7) to 50.3% (1 : 3) (Fig. 2e). The obvious change in the proportion of each solvation cluster is indicative of the effective regulation by the solvent. Compared to SF (Fig. S7), the 1 : 5-type electrolyte using DMSF contains more AGG clusters (43.4%), demonstrating the

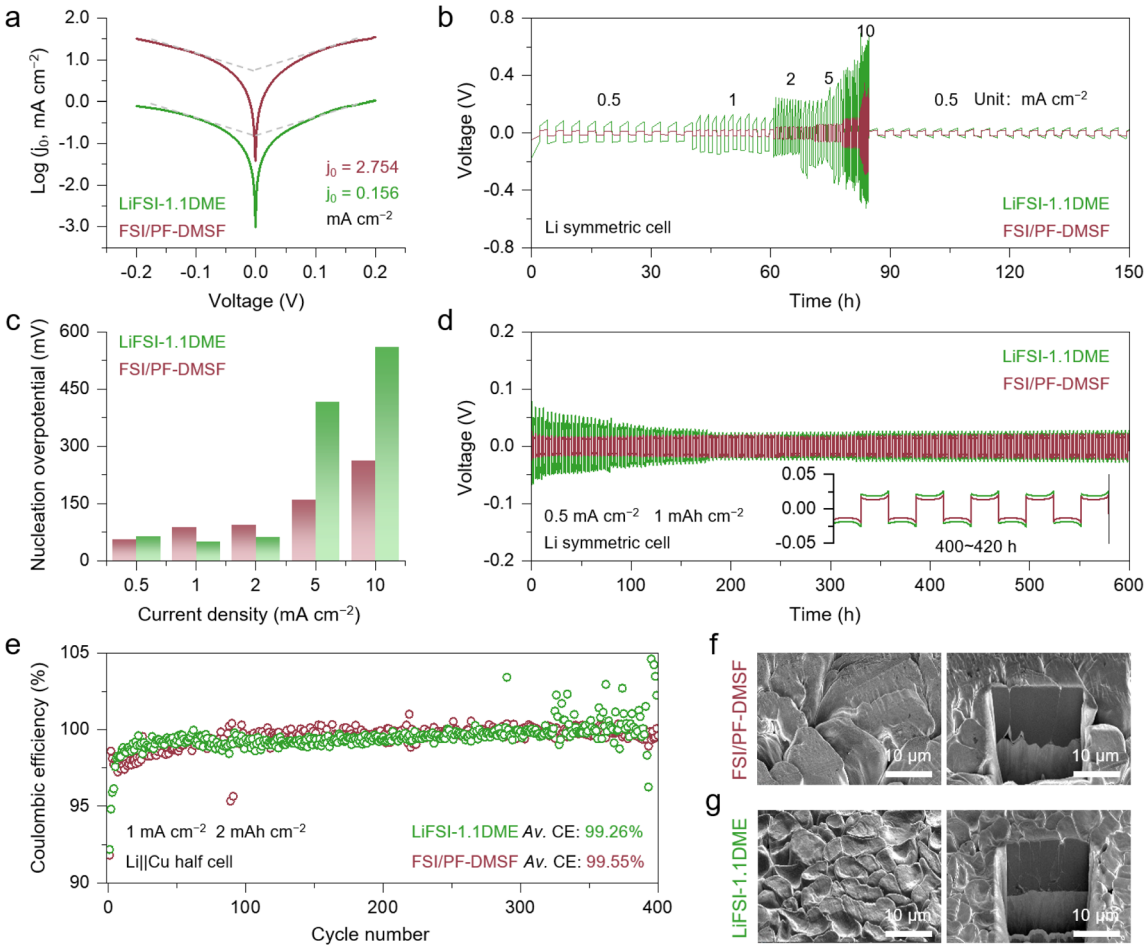

Fig. 3 Interphase kinetics and electrochemical compatibility toward the Li metal anode in the fluorinated sulfonyl-based electrolytes. (a) Tafel plots of Li||Li symmetrical cells and the corresponding exchange current density in the FSI/PF-DMSF and LiFSI-1.1DME electrolytes. (b) Galvanostatic cycling performance of Li||Li symmetrical cells at different current densities using the FSI/PF-DMSF and LiFSI-1.1DME electrolytes. (c) Variation of the Li plating/stripping overpotential at various current densities using the FSI/PF-DMSF and LiFSI-1.1DME electrolytes. (d) Galvanostatic cycling performance of Li||Li symmetrical cells at 0.5 mA cm^{-2} and 1 mAh cm^{-2}. (e) CEs of Li stripping/plating as a function of cycle number tested in Li||Cu half-cells at 0.5 mA cm^{-2} and 1 mAh cm^{-2}. (f and g) Top-view and cross-sectional SEM images of deposited Li using the (f) FSI/PF-DMSF and (g) LiFSI-1.1DME electrolytes.

weak interaction between DMSF and Li ion. In addition, a free DMSF molecule exhibits a stretching vibration band at 1195 cm^{-1}. This band shifts up to 1229 cm^{-1} when DMSF participates in Li^+ solvation. ^1H nuclear magnetic resonance (NMR) spectroscopy was further conducted and shows that the downfield shift in the proton signal of DMSF in FSI/PF-DMSF (0.06 ppm) is noticeably smaller than that in the case of SF in FSI/PF-SF (0.11 ppm) (Fig. 2f), validating the weak DMSF–Li^+ binding. Moreover, according to the molecular dynamics (MD) simulations, the calculated coordination numbers (CNs) between Li^+ and oxygen atoms of DMSF (O_DMSF) and FSI^- (O_FSI^-) were approximately 3.2 and 2.3, respectively. For the SF system, the CN is 3.7 and 1.7, respectively, for the O_SF and O_FSI^- (Fig. S8). The weak DMSF–Li^+ binding could be attributed to the methylation of the nitrogen atom, in which the introduction of $-CH_3$ enhances the steric hindrance effect of DMSF, weakening the coordination of the sulfonyl group with Li ions.

2.3 Li deposition in FSI/PF-DMSF

The reduction reaction (charge transfer) of Li ions typically involves three sequential steps: desolvation, transport through the SEI, and electron transfer.[39,40] Among these, the desolvation process is generally recognized as the rate-determining step. Lower Li-ion desolvation energy barriers typically yield higher exchange current densities (j_0) that benefit uniform Li deposition.[41] In this regard, the high-concentration 1,2-dimethoxyethane (DME)-based electrolyte (LiFSI-1.1DME) was selected as a baseline due to its well-established compatibility with Li anodes.[42–45] The Tafel analysis confirms enhanced kinetics in FSI/PF-DMSF, exhibiting a j_0 of 2.754 mA cm^{-2}, which is 18 times higher than that of LiFSI-1.1DME (0.156 mA cm^{-2}) (Fig. 3a). The fast kinetics imparted by the weak Li-ion solvation of FSI/PF-DMSF play a significant role in maintaining uniform Li deposition.

Galvanostatic rate tests were conducted to evaluate the dendrite-suppressing effect of FSI/PF-DMSF as the current density increased from 0.5 to 10.0 mA cm^{-2}. As shown in Fig. 3b, FSI/PF-DMSF enables stable Li plating/stripping behavior in Li symmetric cells even at 10.0 mA cm^{-2}, while the LiFSI-1.1DME cell exhibits significant voltage fluctuations, especially at high rates. As the current density increases from 0.5 to 10 mA cm^{-2}, the overpotential of Li nucleation in FSI/PF-DMSF changed from 56.5 and 261.4 mV (Fig. 3c and S9). By contrast, the overpotential increase is significant in LiFSI-1.1DME under the same conditions, from 65.0 to 559.4 mV. The galvanostatic cycling performance of the Li metal anode was also improved by using FSI/PF-DMSF (Fig. 3d). The symmetric cell with FSI/PF-DMSF maintains a minimal voltage polarization of 22.9 mV after 600 hours of cycling at 0.5 mA cm^{-2}. However, the polarization of the LiFSI-1.1DME cell is twice that of the FSI/PF-DMSF cell in the initial cycle and gradually decreases over the following cycles (0–200 hours). This long-term process of voltage variation largely corresponds to an increase in the active interface area caused by Li cycling (Fig. S10). For the same reason, the stable voltage fluctuation of the FSI/PF-DMSF cell throughout the cycles is indicative of the effective suppression of dendrite growth and interface degeneration.

To further investigate the compatibility of FSI/PF-DMSF with Li metal, the Li plating/stripping reversibility was evaluated using Li‖Cu half cells at 1 mA cm^{-2} with 2 mAh cm^{-2} Li capacity. As shown in Fig. 3e, both electrolytes exhibit an initial coulombic efficiency (CE) of >92%. For LiFSI-1.1DME, the CE remains stable during the initial 300 cycles, followed by significant fluctuations, indicating that interface damage gradually accumulates with cycling and severely affects electrochemical behavior once a threshold is reached.

Consistent with the results of Li symmetric cells, FSI/PF-DMSF demonstrates improved Li metal compatibility, achieving an average CE of 99.55%. This advantage of FSI/PF-DMSF was more pronounced at higher current densities (Fig. S11).

The morphology of deposited Li was examined using scanning electron microscopy (SEM) and cryogenic-focused ion beam (cryo-FIB) techniques. As shown in Fig. 3f, g and S11, the Li deposited after 5 cycles exhibits bulk, dense, and dendrite-free morphologies in both FSI/PF-DMSF and LiFSI-1.1DME. Notably, the primary particle size obtained from FSI/PF-DMSF is significantly larger than that produced in LiFSI-1.1DME. This is because the low overpotential in FSI/PF-DMSF is beneficial for reducing nucleation sites, promoting the Li deposition layer with a morphology featuring low specific surface area. From the cross-sectional view, the Li deposition in FSI/PF-DMSF exhibits greater compactness than that in LiFSI-1.1DME, where the density of the boundary layer formed at the contact interface of the primary Li deposition particle is higher in LiFSI-1.1DME than in FSI/PF-DMSF. The boundary originates from the SEI, which has anisotropy with Li metal and reduces the electronic conductivity of the Li deposition layer to some extent. Therefore, compared to LiFSI-1.1DME, the Li plating/stripping in FSI/PF-DMSF shows higher stability and reversibility (Fig. S12 and S13), even though there is no obvious formation of Li dendrites in either system.

2.4 The effect of DMSF on SEI formation

The SEI plays a critical role in regulating the Li deposition and enhancing the reversibility of Li metal anodes. Cryogenic transmission electron microscopy (cryo-TEM) reveals that a uniform and thin SEI layer with a thickness of approximately 5.4 nm was formed on the Li metal surface after plating in FSI/PF-DMSF (Fig. S14). The X-ray photoelectron spectroscopy (XPS) depth profiling indicates that the organic content on the FSI/PF-DMSF-derived SEI shows a decreasing trend as the etching depth increases, while the subsurface region is enriched with LiF and Li_2S (Fig. 4a). This result demonstrates the formation of a stratified organic/inorganic SEI structure in FSI/PF-DMSF. By contrast, the SEI induced in the conventional carbonate-based electrolyte (CCE) featured a regular mosaic structure with high organic content (Fig. S15). This SEI has been proven to be difficult to effectively regulate Li metal cycling. In the case of the FSI/PF-DMSF-derived SEI, the electron-insulating organic outer layer effectively passivates the electrode surface and suppresses

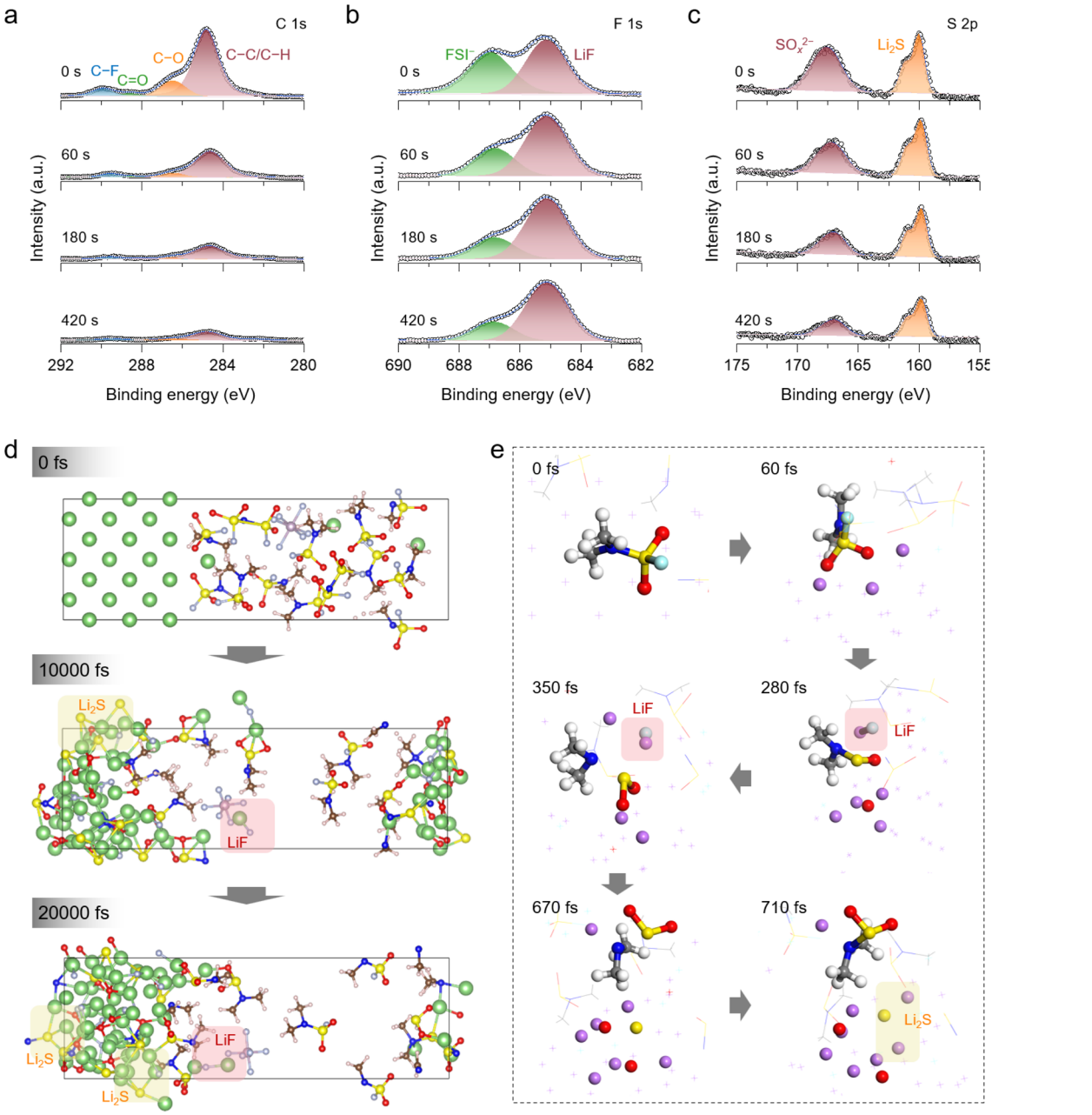

Fig. 4 Interphase chemistry and its formation mechanism in the FSI/PF-DMSF electrolyte. (a–c) XPS spectra of the SEI on the Li anode electrode of Li||NCM811 full cells after 20 cycles in the FSI/PF-DMSF electrolyte. (d) Snapshots of reduction decomposition of DMSF in the FSI/PF-DMSF electrolyte from AIMD simulation. (e) AIMD simulation of the rich-LiF/Li_2S SEI formation process on the Li metal surface.

side reactions, whereas the ion-conductive inner layer rich in LiF and Li_2S facilitates rapid Li-ion diffusion and promotes uniform Li-ion deposition.

Notably, in the S 2p spectra, inorganic sulfur-containing components in the SEI of FSI/PF-DMSF are distinct from those generated by the reduction of FSI^- in LiFSI-1.1DME (Fig. 4b). The sulfur-containing inorganic components in FSI/PF-DMSF are single, with only Li_2S signals detected. In contrast, the SEI of LiFSI-1.1DME shows diverse reduction products of FSI^- anions and presents a mosaic structure (Fig. S16). These results indicate that the Li_2S formed in FSI/PF-DMSF is derived from the decomposition of DMSF rather than FSI^-, which is in line with the CV observation that DMSF has a high reduction potential and could preferentially passivate the Li metal anode to reduce the decomposition of anions.

The *ab initio* molecular dynamics (AIMD) simulation was conducted to elucidate the decomposition process of FSI/PF-DMSF on the Li metal surface (Fig. 4c). In the initial stage (60 fs), the DMSF molecule adsorbs onto the Li metal surface and then undergoes reduction, decomposition, and de-fluorination, forming LiF on the Li metal surface (280 fs). Between 280 and 670 fs, the $(CH_3)N–SO_2^-$ group moves closer to the Li metal interface and cleaves into $(CH_3)N^-$ and SO_2^- fragments. By 710 fs, SO_2^- further decomposes, resulting in the formation of Li_2S

on the Li metal surface. As shown in Fig. 4d, the reduction of FSI/PF-DMSF mainly involves the de-fluorination and de-sulfurization of the DMSF molecule, while the FSI^- anion is less participating in these reactions as a result of the calculation. This further indicates the preferential decomposition behavior of DMSF. Combined with the XPS results, it can be confirmed that methylation promotes the decomposition of DMSF, forming a stratified organic–inorganic SEI with a rich LiF/Li_2S inner layer to effectively facilitate the interfacial Li-ion kinetics and enable uniform Li deposition with large size.

2.5 Cycling of the full cell with FSI/PF-DMSF

The CCE and FSI/PF-SF were used as references to assess the role of FSI/PF-DMSF in the improvement of the cycling performance of the Li metal full cell. The NCM811 mass loading is 17.8 mg cm^{-2}, and the N/P ratio is ~2.5. The cycling of Li||NCM811 coin-type cells was carried out at 25 °C, with a charge cut-off voltage of 4.5 V. As shown in Fig. 5a, the FSI/PF-DMSF cell delivers a capacity of 3.5 mAh at 0.5C and excellent cycling stability, maintaining an 80% capacity retention after 850 cycles. The stable voltage profiles of the FSI/PF-DMSF cell over cycles indicate not only a robust Li metal interface with high Li cycling reversibility but also a significant restriction of the electrolyte parasitic reaction on the cathode side at high voltages (Fig. 5b). It can be seen in Fig. S15 that FSI-DMSF without the $LiPF_6$ additive only supports stable operation of the Li||NCM811 cell up to 4.3 V. When the voltage is increased to 4.5 V, the cycling of the FSI-DMSF cell declines rapidly due to the aluminum corrosion (Fig. S17 and S18). This result emphasizes that the high-voltage performance of FSI/PF-DMSF cannot be achieved without the help of $LiPF_6$. For the CCE and FSI/PF-SF cell, their performance basically fails within 200 cycles due to the unstable interface (Fig. 5a and S19), where the corrosion of the Li metal caused by the α-H of SF is a direct reason for the drop in cell capacity.

The temperature range for the operation of the FSI/PF-DMSF cell was also investigated as shown in Fig. 5c. As expected, 3.6 mAh of the initial capacity is output at 60 °C, and this cell also shows a capacity retention of 85.0% after 100 cycles. This high-temperature performance of the cell could be attributed to the

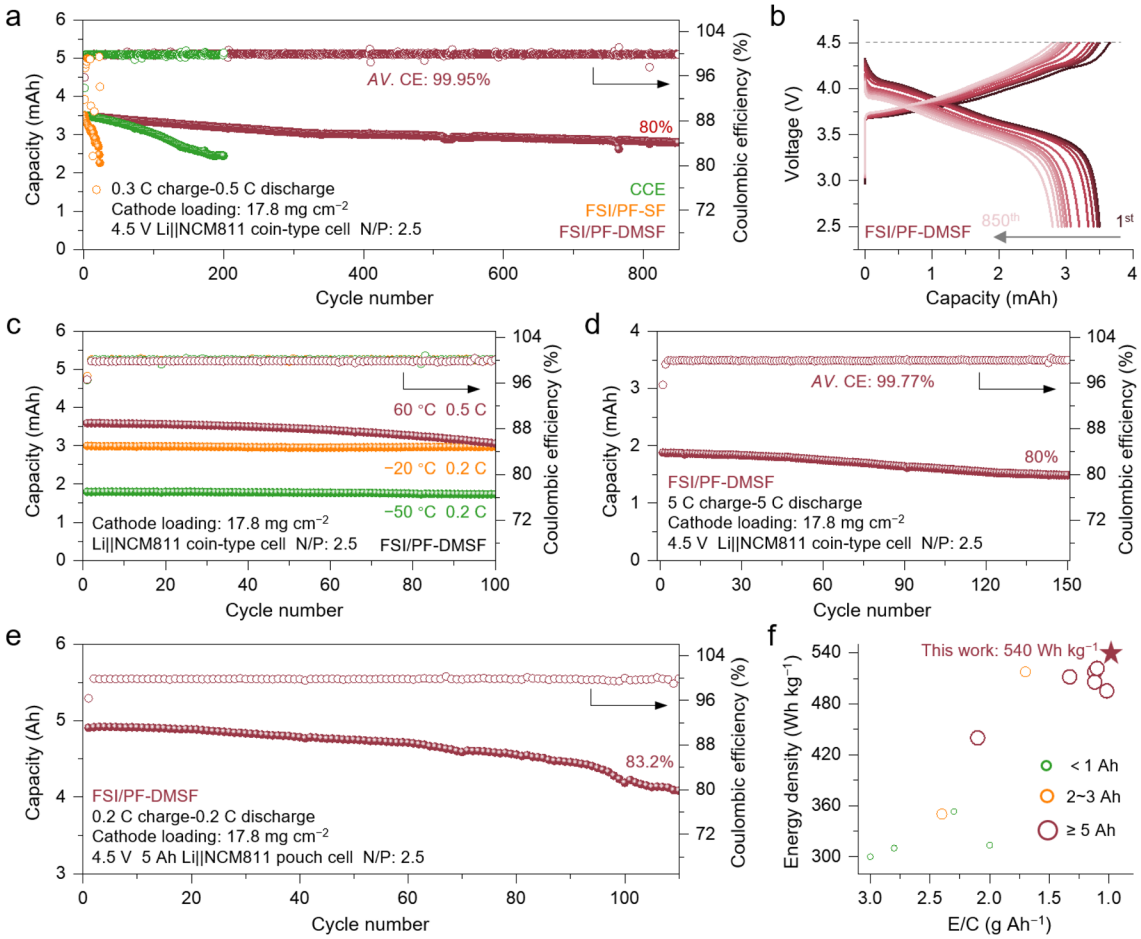

Fig. 5 Electrochemical performances of Li||NCM811 full cells under extreme conditions. (a) Long-cycling performance of the Li||NCM811 coin cell in different electrolytes, (b) the charge–discharge curves of the cell using FSI/PF-DMSF electrolyte in (a). (c) Long-cycling performance of Li||NMC811 cells using FSI/PF-DMSF electrolyte at 60 °C, −20 °C, and −50 °C. (d) Long-cycling performance of the Li||NCM811coin cells with FSI/PF-DMSF electrolyte at 5.0C charge/5.0C discharge. (e) Long-cycling performance of a 5 Ah Li||NCM811 pouch cell with FSI/PF-DMSF electrolyte. (f) Comparisons of the state-of-the-art performance in terms of energy density (criteria: energy density ≥300 Wh kg^{-1} and cycle life ≥100 cycles) and the E/C ratio in this work and recently reported Li metal pouch cells.

stable chemical structure of DMSF and the SEI. At low temperature, the Li||NCM811 cell with FSI/PF-DMSF shows a capacity retention of 85.6% at −20 °C compared to the reversible capacity derived at 25 °C. Meanwhile, the cycling remains stable without any significant capacity decline. In addition, when the cell is tested at −50 °C, a reversible capacity of around 1.8 mAh was achieved (51.4% of the 25 °C-capacity output), and this cell can stably operate over 100 cycles (Fig. S20). Obviously, the weak desolvation barrier stemmed from the steric hindrance effect of DMSF ensures favorable Li-ion kinetics at low temperatures. The SEI induced by FSI/PF-DMSF, in addition, could promote the interfacial Li-ion transport and stabilize the Li metal interface when cycled at low temperatures. Therefore, FSI/PF-DMSF enables the cell to operate over a wide temperature range of −50 to 60 °C.

Given that the improved performance of the FSI/PF-DMSF cell at low temperature arises from the enhanced kinetics imparted by DMSF, the fast-charging cycling of the cell with FSI/PF-DMSF is also worth investigating. As shown in Fig. 5d and S21, although polarization is increased, the Li||NCM811 cell with FSI/PF-DMSF still delivers a capacity of 2.0 mAh (135.5 mAh g^{-1}) at 5C. Moreover, 83.2% of the reversible capacity was retained after 150 cycles at 5C, with an average CE of 99.77% (Fig. S22), demonstrating the versatility of the electrolyte by using DMSF, including high voltage, wide operating temperature range, and fast charging.

Furthermore, an industrial-level evaluation of FSI/PF-DMSF was performed by testing 5 Ah Li||NCM811 pouch cells. From the result shown in Fig. 5f, this pouch cell attains an energy density of 540 Wh kg^{-1} based on total cell weight (Table S2), meeting the targets outlined by the U.S. Battery500 project. The cell also maintained over 83% capacity retention throughout 110 cycles, with only a marginal increase in polarization observed during continuous cycling, which can also support pouch cell cycling at 2C (Fig. S23). Notably, PTE-PE-SPE also provides high-safety performance for the high-energy LMBs. As shown in Fig. S24, the fully charged (4.5 V, after cycling) Li||NCM811 pouch cell did not catch fire during a nail penetration process. Under the benchmark conditions of energy density ≥300 Wh kg^{-1} and cycle life ≥100 cycles, this 5 Ah pouch cell shows an obvious advantage by using FSI/PF-DMSF, outperforming the Li metal batteries reported in the related literature (Fig. 5g and Table S3).

3 Conclusions

In summary, we designed and systematically evaluated a novel fluorinated sulfonyl-based electrolyte (FSI/PF-DMSF). The molecular structure of DMSF incorporates monofluoro and dimethyl groups that act in synergy, conferring distinctive electronic and steric effects. This effect not only leads to the delocalization of the electron cloud density, forming a weak solvation structure, but also overcomes the high viscosity and poor wettability issues of traditional sulfonyl-based electrolytes, thereby facilitating the rapid de-solvation of Li^+. The interfacial reaction process reveals that this unique effect also promotes solvent-dominated reduction decomposition, generating a SEI dominated by rich LiF and Li_2S, which can effectively protect the Li metal anode from further side reactions. As a result, a 50 μm Li||NCM811 cell with a DMSF-derived SEI achieved extremely stable cycling to operate over 850 cycles (80% retention) at 4.5 V. The full cell delivers a specific capacity of 1.7 mAh cm^{-2} at −50 °C and could also operate reversibly for 100 cycles at 60 °C. Furthermore, an industrial 5 Ah Li||NCM811 pouch cell achieves a high energy density of 540 Wh kg^{-1} with 80.3% capacity retention after 110 cycles. This study extends the application of sulfonyl-based electrolytes to batteries operating under extreme conditions and provides a valuable framework for future electrolyte design.

Author contributions

Jinmin Wang: design and execution of the experiments and preparation of the article draft. Shuang Wei: theoretical calculations. Mingming Fang: design of experiments, supervision, project administration, funding acquisition, writing – reviewing and editing. Angye Li, Qian Zheng, Xubing Dong, Yuanmao Chen and Kang Yuan: validation, data curation. Xinyang Yue: supervision, writing – reviewing and editing. Zheng Liang: supervision, project administration, funding acquisition, writing – reviewing and editing.

Conflicts of interest

There are no conflicts to declare.

Data availability

The data supporting this study are available within the article and the supplementary information (SI). Supplementary information: detailed methods and additional data/results. See DOI: https://doi.org/10.1039/d5sc09242f.

Acknowledgements

This work was financially supported by the National Natural Science Foundation of China (Grant No. 22509121), Henan Yujing Energy Technology (Grant No. 23H010101832), Fundamental Research Funds for the Central Universities (25X010202131), Shanghai PMSM Technology (Grant No. 21H010101815), and China Postdoctoral Science Foundation (Grant No. 2024M751952 and GZC20240991). The authors acknowledge Shanghai TANSUO Testing and Inspection Company for Raman characterization, AIMD simulations and SEM characterization.

References

1 D.-H. Liu, Z. Bai, M. Li, A. Yu, D. Luo, W. Liu, L. Yang, J. Lu, K. Amine and Z. Chen, *Chem. Soc. Rev.*, 2020, **49**, 5407–5445.
2 Y. Liu, X. Tao, Y. Wang, C. Jiang, C. Ma, O. Sheng, G. Lu and X. W. Lou, *Science*, 2022, **375**, 739–745.
3 H. Huang, Y. Hu, Y. Hou, X. Wang, Q. Dong, Z. Zhao, M. Ji, W. Zhang, J. Li, J. Xie, H. Guo, X. Han, X. Ouyang and W. Hu, *Nature*, 2025, **644**, 660–667.

4 R. Li, H. Zhang, S. Zhang, Y. Li, R. Guo, H. Pei, M. Yang, J. Zhang, L. Chen, X. Xiao, L. Chen, Y. Shen, T. Deng and X. Fan, *Nat. Energy*, 2025, **10**, 1155–1165.
5 I. R. Choi, Y. Chen, A. Shah, J. Florian, C. Serrao, J. Holoubek, H. Lyu, E. Zhang, J. H. Lee, Y. Lin, S. C. Kim, H. Park, P. Zhang, J. Lee, J. Qin, Y. Cui and Z. Bao, *Nat. Energy*, 2025, **10**, 365–379.
6 W.-h. Hou, Y. Ou, T. Zeng, Q. Feng, Q. Cao, P. Zhou, Y. Xia, X. Song, W. Zhang, Y. Lu, S. Yan, H.-Y. Zhou, H. Zhou, H. Liu, F. Liu and K. Liu, *Energy Environ. Sci.*, 2024, **17**, 8325–8336.
7 Z. Zhang, Y. Li, R. Xu, W. Zhou, Y. Li, S. T. Oyakhire, Y. Wu, J. Xu, H. Wang, Z. Yu, D. T. Boyle, W. Huang, Y. Ye, H. Chen, J. Wan, Z. Bao, W. Chiu and Y. Cui, *Science*, 2022, **375**, 66–70.
8 S. Ko, Y. Yamada and A. Yamada, *Joule*, 2021, **5**, 998–1009.
9 X. Yue, J. Zhang, Y. Dong, Y. Chen, Z. Shi, X. Xu, X. Li and Z. Liang, *Angew. Chem., Int. Ed.*, 2023, **135**, e202302285.
10 M. Fang, X. Yue, Y. Dong, Y. Chen and Z. Liang, *Joule*, 2024, **8**, 91–103.
11 P. Ding, H. Yuan, L. Xu, L. Wu, H. Du, S. Zhao, D. Yu, Z. Qin, H. Liu, Y. Li, X. Zhang, H. Yu, M. Tang, Y. Ren, L. Li and C. W. Nan, *Adv. Mater.*, 2024, **37**, 2413654.
12 Q. Xu, T. Li, Z. Ju, G. Chen, D. Ye, G. I. N. Waterhouse, Y. Lu, X. Lai, G. Zhou, L. Guo, K. Yan, X. Tao, H. Li and Y. Qiu, *Nature*, 2025, **637**, 339–346.
13 Y. Wang, Y. Ni, S. Xu, Y. Lu, L. Shang, Z. Yang, K. Zhang, Z. Yan, W. Xie and J. Chen, *J. Am. Chem. Soc.*, 2025, **147**, 10772–10783.
14 Z. Yu, H. Wang, X. Kong, W. Huang, Y. Tsao, D. G. Mackanic, K. Wang, X. Wang, W. Huang, S. Choudhury, Y. Zheng, C. V. Amanchukwu, S. T. Hung, Y. Ma, E. G. Lomeli, J. Qin, Y. Cui and Z. Bao, *Nat. Energy*, 2020, **5**, 526–533.
15 A.-M. Li, O. Borodin, T. P. Pollard, W. Zhang, N. Zhang, S. Tan, F. Chen, C. Jayawardana, B. L. Lucht, E. Hu, X.-Q. Yang and C. Wang, *Nat. Chem.*, 2024, **16**, 922–929.
16 M. Li, Y. Liu, X. Yang, Q. Zhang, Y. Cheng, L. Deng, Q. Zhou, T. Cheng and M. D. Gu, *Adv. Mater.*, 2024, **36**, 2404271.
17 J. Peng, H. Zhang, Z. Zeng, H. Zhang, H. Pei, Q. Wu, Y. Shen, R. Guo, S. Cheng and J. Xie, *Adv. Mater.*, 2025, e09109.
18 J. Wang, Y. Yamada, K. Sodeyama, C. H. Chiang, Y. Tateyama and A. Yamada, *Nat. Commun.*, 2016, **7**, 12032.
19 J. Wang, Y. Yamada, K. Sodeyama, E. Watanabe, K. Takada, Y. Tateyama and A. Yamada, *Nat. Energy*, 2017, **3**, 22–29.
20 E. Zhang, Y. Chen, J. Holoubek, Z. Yu, W. Zhang, H. Lyu, I. R. Choi, S. C. Kim, C. Serrao, Y. Cui and Z. Bao, *Proc. Natl. Acad. Sci. U. S. A.*, 2025, **122**, 2418623122.
21 Y. Zhao, T. Zhou, M. Mensi, J. W. Choi and A. Coskun, *Nat. Commun.*, 2023, **14**, 299.
22 Z. Yu, P. E. Rudnicki, Z. Zhang, Z. Huang, H. Celik, S. T. Oyakhire, Y. Chen, X. Kong, S. C. Kim, X. Xiao, H. Wang, Y. Zheng, G. A. Kamat, M. S. Kim, S. F. Bent, J. Qin, Y. Cui and Z. Bao, *Nat. Energy*, 2022, **7**, 94–106.
23 Q. Wang, C. Zhao, J. Wang, Z. Yao, S. Wang, S. G. H. Kumar, S. Ganapathy, S. Eustace, X. Bai, B. Li and M. Wagemaker, *Nat. Commun.*, 2023, **14**, 440.
24 S. C. Kim, J. Wang, R. Xu, P. Zhang, Y. Chen, Z. Huang, Y. Yang, Z. Yu, S. T. Oyakhire, W. Zhang, L. C. Greenburg, M. S. Kim, D. T. Boyle, P. Sayavong, Y. Ye, J. Qin, Z. Bao and Y. Cui, *Nat. Energy*, 2023, **8**, 814–826.
25 X. Fan and C. Wang, *Chem. Soc. Rev.*, 2021, **50**, 10486–10566.
26 W. Yang, J. Cai, C. Xu, A. Chen, Y. Wang, Y. Shi, P. He and H. Zhou, *Adv. Mater.*, 2025, **37**, 2505285.
27 T.-L. Chen, M. Liu, X.-Y. Fan, Y.-H. Feng, Q. Liu, X.-R. Liu, H. Xin and P.-F. Wang, *ACS Energy Lett.*, 2024, **9**, 5452–5460.
28 X. Dong, M. Fang, M. Li, K. Yuan, X. Zhang, X. Yue and Z. Liang, *CCS Chem.*, 2025, 1–13.
29 S. Xue, Y. Zhou, X. Liu and M. He, *J. Energy Storage*, 2023, **64**, 107137.
30 F. Wu, J. Xiang, L. Li, J. Chen, G. Tan and R. Chen, *J. Power Sources*, 2012, **202**, 322–331.
31 T. Zhang, W. Porcher and E. Paillard, *J. Power Sources*, 2018, **395**, 212–220.
32 X. Ren, S. Chen, H. Lee, D. Mei, M. H. Engelhard, S. D. Burton, W. Zhao, J. Zheng, Q. Li, M. S. Ding, M. Schroeder, J. Alvarado, K. Xu, Y. S. Meng, J. Liu, J.-G. Zhang and W. Xu, *Chem*, 2018, **4**, 1877–1892.
33 R. Liu, Y. S. Xu, R. Zhou, S. J. Tan, Y. N. Li, S. J. Jiang, S. Xin, Y. G. Guo and F. F. Cao, *Angew. Chem., Int. Ed.*, 2024, **64**, e202416610.
34 W. Xue, M. Huang, Y. Li, Y. G. Zhu, R. Gao, X. Xiao, W. Zhang, S. Li, G. Xu, Y. Yu, P. Li, J. Lopez, D. Yu, Y. Dong, W. Fan, Z. Shi, R. Xiong, C.-J. Sun, I. Hwang, W.-K. Lee, Y. Shao-Horn, J. A. Johnson and J. Li, *Nat. Energy*, 2021, **6**, 495–505.
35 L.-Q. Wu, Z. Li, H. Li, J.-Y. Zhang, Y. Li, S.-X. Ren, Z.-Y. Fan, X.-T. Wang, K. Li, Z. Liu, J. Zhang, J.-C. Yang, Y.-W. Li, S.-H. Bo and Q. Zhao, *J. Am. Chem. Soc.*, 2025, **147**, 16506–16521.
36 Y. Roh, H. Kwon, J. Baek, C. Park, S. Kim, K. Hwang, A. R. Ha, S. Ha, J. Song and H. T. Kim, *Adv. Energy Mater.*, 2024, **15**, 2403944.
37 S. Chen, J. Zheng, D. Mei, K. S. Han, M. H. Engelhard, W. Zhao, W. Xu, J. Liu and J. G. Zhang, *Adv. Mater.*, 2018, **30**, e1706102.
38 D. J. Yoo, S. Yang, K. J. Kim and J. W. Choi, *Angew. Chem., Int. Ed.*, 2020, **59**, 14869–14876.
39 T. R. Jow, S. A. Delp, J. L. Allen, J.-P. Jones and M. C. Smart, *J. Electrochem. Soc.*, 2018, **165**, A361–A367.
40 S.-Y. Sun, X.-Q. Zhang, Y.-N. Wang, J.-L. Li, Z. Zheng and J.-Q. Huang, *Mater. Today*, 2024, **77**, 39–65.
41 D. T. Boyle, S. C. Kim, S. T. Oyakhire, R. A. Vilá, Z. Huang, P. Sayavong, J. Qin, Z. Bao and Y. Cui, *J. Am. Chem. Soc.*, 2022, **144**, 20717–20725.
42 X. Cao, H. Jia, W. Xu and J.-G. Zhang, *J. Electrochem. Soc.*, 2021, **168**, 010522.
43 Y. Yamada, J. Wang, S. Ko, E. Watanabe and A. Yamada, *Nat. Energy*, 2019, **4**, 269–280.
44 S. Jiao, X. Ren, R. Cao, M. H. Engelhard, Y. Liu, D. Hu, D. Mei, J. Zheng, W. Zhao, Q. Li, N. Liu, B. D. Adams, C. Ma, J. Liu, J.-G. Zhang and W. Xu, *Nat. Energy*, 2018, **3**, 739–746.
45 J. Qian, W. A. Henderson, W. Xu, P. Bhattacharya, M. Engelhard, O. Borodin and J. G. Zhang, *Nat. Commun.*, 2015, **6**, 6362.